Inorganic Chemistry

Article

pubs.acs.org/IC

2-(Phenylazo)pyridineplatinum(II) Catecholates Showing Photocytotoxicity, Nuclear Uptake, and Glutathione-Triggered Ligand Release

Koushambi Mitra,[†] Shilpa Patil,[‡] Paturu Kondaiah,*[,‡] and Akhil R. Chakravarty*[,†]

[†]Department of Inorganic and Physical Chemistry and [‡]Department of Molecular Reproduction and Genetics, Indian Institute of Science, Bangalore 560012, India

Supporting Information

ABSTRACT: Platinum(II) complexes [Pt(pap)(an-cat)] (**1**) and [Pt(pap)(py-cat)] (**2**) with 2-(phenylazo)pyridine (pap), 4-[2-[(anthracen-9-ylmethylene)amino]ethyl]benzene-1,2-diol (H_2an-cat), and 4-[2-[(pyren-1-ylmethylene)amino]ethyl]-benzene-1,2-diol (H_2py-cat) were prepared, and their photo-induced cytotoxicity was studied. The complexes were found to release catecholate ligand in the presence of excess glutathione (GSH), resulting in cellular toxicity in the cancer cells. The catecholate complex [Pt(pap)(cat)] (**3**) was prepared and used as a control. Complex **3**, which is structurally characterized by X-ray crystallography, has platinum(II) in a distorted square-planar geometry. The complexes are redox-active, showing responses near 0.6 and 1.0 V versus SCE in *N*,*N*-dimethylformamide/0.1 M tetrabutylammonium perchlorate corresponding to a two-step catechol oxidation process and at −0.3 and −1.3 V for reduction of the pap ligand. Complex **1** showed remarkable light-induced cytotoxicity in HaCaT (human skin keratinocytes) and MCF-7 (human breast cancer) cells, giving IC_{50} value of ∼5 μM in visible light of 400−700 nm and >40 μM in the dark. The 2′,7′-dichlorofluorescein diacetate (DCFDA) assay showed the generation of reactive oxygen species (ROS), which seems to trigger apoptosis, as is evident from the annexin V−fluorescein isothiocyanate (FITC)/propidium iodide (PI) assay. The fluorescence microscopic images showed significant nuclear localization of the complexes and free ligands. A mechanistic study revealed possible reduction of the coordinated azo bond of pap by cellular GSH, releasing the catecholate ligand and resulting in remarkable photochemotherapeutic action of the complexes.

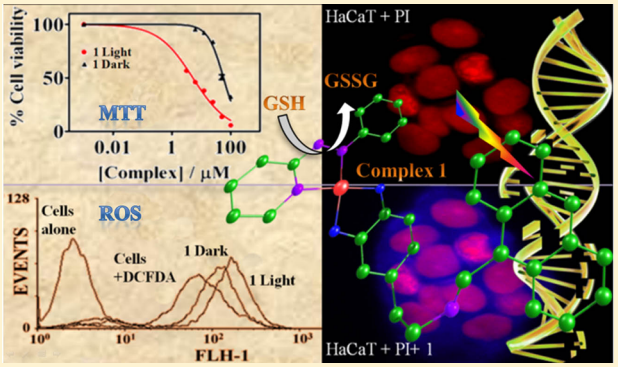

1. INTRODUCTION

Specificity and efficacy are two major requirements for an anticancer drug.[1−3] Platinum-based chemotherapeutic agents such as cisplatin, carboplatin, and oxaliplatin are known to show undesirable side effects and procured resistances.[4−6] To augment the efficacy of the platinum(II) drugs, Lippard and co-workers have reported kinetically more stable platinum(IV) prodrugs, generating cytotoxic platinum(II) complexes upon cellular reduction at the targeted cancer cells.[7−9] Dual targeting of these prodrugs by modifying the axial ligands has shown remarkable antiproliferative activities in targeted chemotherapy.[10−15] Using an alternative approach based on photodynamic therapy (PDT), Sadler and co-workers have shown that additional selectivity can be achieved by activating a platinum(IV) prodrug by light exposure specifically within the target tumor cells, thus not harming the unexposed normal cells.[16−18] Although metal-based photocytotoxic agents have emerged as potential alternatives to the PDT drug Photofrin, the chemistry of photocytotoxic platinum(II) complexes is virtually unknown.[16−27]

The present work stems from our interest to design photoactive platinum(II) prodrugs in a ternary structure in which we have used 2-(phenylazo)pyridine (pap) and catechol derivatives to achieve ligand release by cellular glutathione (GSH), generating a pap-based cisplatin analogue as the cytotoxin and photosensitizer-appended released catechol derivatives as the phototoxin. GSH as a nonprotein thiol is a key regulator for various biological processes, and an elevated level of GSH could act as a potent tumor target.[28,29] Earlier reports have shown that half-sandwich organometallic (arene)-ruthenium(II) complexes are highly cytotoxic because of the redox reactions of the metal-coordinated azo ligands and GSH.[30−32] Herein, we report two platinum(II) complexes, viz., [Pt(pap)(an-cat)] (**1**) and [Pt(pap)(py-cat)] (**2**), where pap is 2-(phenylazo)pyridine, H_2an-cat is 4-[2-[(anthracen-9-ylmethylene)amino]ethyl]benzene-1,2-diol, and H_2py-cat is 4-[2-[(pyren-1-ylmethylene)amino]ethyl]benzene-1,2-diol (Scheme 1). The choice of pap is based on its ability to undergo redox reaction with GSH upon coordination to a metal center. The catecholate ligand was modified by appending anthracene or pyrene as the photosensitizer moiety. The

Received: September 24, 2014
Published: December 12, 2014

   dx.doi.org/10.1021/ic502317z | *Inorg. Chem.* 2015, 54, 253−264

Scheme 1. Complexes 1−3 and the Ligands Used

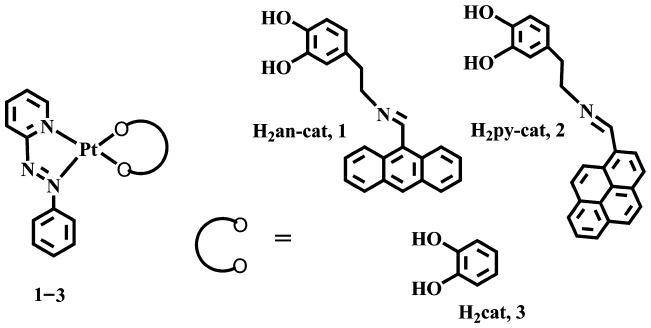

presence of catechol has resulted in an intense band in the near-IR region. The emissive property of the anthracenyl and pyrenyl complexes has enabled us to trace the complexes within the tumor cells by cellular imaging. The catechol complex [Pt(pap)(cat)] (**3**), where H_2cat is catechol, was prepared and used as a control. Significant results of this work include the high photocytotoxicity of complex **1** in both HaCaT and MCF-7 cells in visible light with low dark toxicity and significant nuclear localization of the complexes. The PDT effect is comparable to that of Photofrin. The observation of GSH-induced catecholate ligand release resulting in the formation of a pap-bound platinum(II) species and photoactive catecholate derivative is remarkable.

2. EXPERIMENTAL SECTION

Materials and Measurements. Potassium tetrachloroplatinate was purchased from Arora Matthey, India. Supercoiled (SC) pUC19 DNA (cesium chloride purified) was purchased from Bangalore Genie (India). All other reagents and chemicals were obtained from Sigma-Aldrich, USA. Solvents were purified by known procedures.[33] A tris(hydroxymethyl)aminomethane−HCl (Tris-HCl) buffer solution was prepared using deionized and sonicated triple-distilled water. The complexes were synthesized under a nitrogen atmosphere using a Schlenk line. 2-(Phenylazo)pyridine (pap) and the precursor complex dichloro[2-(phenylazo)pyridine]platinum(II), namely, [Pt(pap)Cl_2], were prepared following literature methods.[34] The catecholate ligands were synthesized by treating dopamine hydrochloride (0.5 g, 2.63 mmol) in ethanol (5 mL), neutralized with few drops of freshly distilled triethylamine, with the corresponding aldehyde (Scheme S1 in the Supporting Information, SI). The solution was stirred for 2 h at room temperature under a nitrogen atmosphere, and the resulting bright-yellow precipitate was isolated, washed with a small amount of ethanol and ether, and dried in a vacuum (see Figures S1−S6 in the SI for the characterization data).

Elemental analysis was done using a Thermo Finnigan FLASH EA 1112 CHNS analyzer. The IR and UV−visible spectra were recorded on FT-IR Bruker Alpha and PerkinElmer Lambda 650 spectrometers, respectively. Electrospray ionization mass spectrometry (ESI-MS) measurements were done using an Agilent 6538 Ultra High Definition Accurate Mass-Q-TOF (LC-HRMS) instrument. The NMR spectra were recorded at room temperature using a Bruker Avance 400 (400 MHz) NMR spectrometer. Cyclic voltammetric measurements were done at 25 °C using an EG&G PAR model 253 VersaStat potentiostat/galvanostat with electrochemical analysis software 270 and a three-electrode setup consisting of a a glassy carbon working, a platinum wire auxiliary, and a saturated calomel reference electrode (SCE) in *N*,*N*-dimethylformamide (DMF) as the solvent and tetrabutylammonium perchlorate (TBAP; 0.1 M) as the supporting electrolyte. Molar conductivity was measured using a Control Dynamics (India) conductivity meter. Viscometric measurements were performed with a Schott AVS 310 automated viscometer. Fluorescent-activated cell sorting (FACS) analysis was done using a Calibur [Becton−Dickinson (BD)] cell analyzer at the FL1 channel. Imaging studies were performed with an Olympus IX 81 fluorescence microscope. The platinum content was measured by an inductively coupled plasma mass spectroscopy (ICP-MS) method using a Thermo X series II instrument. High-performance liquid chromatography (HPLC) was performed with a Waters Alliance System with *EMPOWER* 3 software (Waters Corp., Milford, MA) consisting of a 2695 separation module and a 2996 photodiode-array detector. The samples were injected (30 μL) into the reversed-phase column (Lichrosphere 60, RP-select B, 5 mm), with a flow rate of 1 mL min^{-1}, eluted with an acetonitrile/water gradient maintaining the acetonitrile percentage as 80% for 17 min and 10% for 8 min, and detected at 275 nm.

Synthesis. The complexes were prepared by following a common procedure (Scheme S2 in the SI) in which [Pt(pap)Cl_2] (50 mg, 0.11 mmol for **1**; 200 mg, 0.44 mmol for **2**; 100 mg, 0.22 mmol for **3**) dissolved in 20 mL of methanol and purged with nitrogen was reacted with the catecholate ligand (38 mg, 0.11 mmol, H_2an-cat; 200 mg, 0.54 mmol, H_2py-cat; 30 mg, 0.27 mmol, H_2cat) in 10 mL of methanol, followed by the addition of freshly distilled triethylamine (1 mL). The solution was stirred at room temperature in the dark for 12 h, during which the color changed from red to green. The solution was then evaporated under reduced pressure, the resulting crude green precipitate was dissolved in a small volume of acetonitrile, and the solid was precipitated with diethyl ether. The solid was isolated and washed with diethyl ether and dried in a vacuum.

[Pt(pap)(an-cat)] (1). Yield: 65 mg (0.09 mmol, ∼80%). Anal. Calcd for $C_{34}H_{26}N_4O_2Pt$ (M_w = 717.69): C, 56.90; H, 3.65; N, 7.81. Found: C, 56.82; H, 3.72; N, 7.77. ^{1}H NMR (400 MHz, DMSO-d_6): δ 9.49 (b, 1H), 9.27 (s, 1H, imine C═H), 9.04 (d, 2H), 8.65 (s, 1H), 8.40 (b, 2H), 8.32 (d, 1H, J = 5.2 Hz), 8.09 (m, 2H), 7.76−7.65 (br, 5H), 7.49 (m, 4H), 6.89−6.76 (br, 2H), 6.44 (d, 1H, J = 7.6 Hz), 4.14 (d, 2H, J = 6 Hz), 3.40 (d, 2H, J = 7.6 Hz) [br, broad; s, singlet; d, doublet; m, multiplet]. ^{13}C NMR (100 MHz, DMSO-d_6): δ 161.04, 133.16, 132.26, 131.58, 130.26, 130.07, 129.48, 127.39, 126.75, 126.30, 126.022, 125.34, 124.37, 58.64, 31.59. ESI-MS (in MeCN): m/z 718.2000 ([M + H]$^+$, 100%). Calcd: m/z 718.1782. UV−visible in 10% dimethyl sulfoxide (DMSO)/phosphate buffered saline (PBS) (pH 7.2) [λ, nm (ε, M^{-1} cm^{-1})]: 825 (1660), 390 (7980), 370 (8040). Selected IR data (cm^{-1}): 1594 (m), 1448 (s), 1290 (s), 770 (s), 650 (w) (s, strong; m, medium; w, weak). Molar conductance in DMF at 298 K (Λ_M): 34 S m^2 M^{-1}.

[Pt(pap)(py-cat)] (2). Yield: 240 mg (0.32 mmol, ∼75%). Anal. Calcd for $C_{36}H_{26}N_4O_2Pt$ (M_w = 741.71): C, 58.30; H, 3.53; N, 7.55. Found: C, 58.13; H, 3.64; N, 7.38. ^{1}H NMR (400 MHz, DMSO-d_6): δ 9.42 (d, J = 9.6 Hz, 2H), 9.28 (s, 1H, imine C═H), 9.05 (m, 1H), 8.63−8.10 (m, 10H), 7.61 (br, 5H), 6.85−6.74 (m, 2H), 6.43 (d, J = 8 Hz, 1H), 4.01 (t, J = 8 Hz, 2H), 3.0 (t, J = 8 Hz, 2H) (t, triplet). ^{13}C NMR (100 MHz, DMSO-d_6): δ 163.59, 154.04, 135.91, 131.66, 131.61, 131.43, 131.18, 130.78, 128.25, 128.20, 27.91, 127.85, 125.86, 124.65, 123.49, 52.95, 46.41. ESI-MS (in MeCN): m/z 742.1728 ([M + H]$^+$, 100%). Calcd: m/z 742.1782. UV−visible in 10% DMSO/PBS (pH 7.2) [λ, nm (ε, M^{-1} cm^{-1})]: 788 (2000), 395 (10360), 370 (12000), 348 (11640), 288 (18650). Selected IR data (cm^{-1}): 1587 (m), 1288 (s), 1226 (s), 843 (s), 766 (s), 550(s). Molar conductance in DMF at 298 K (Λ_M): 40 S m^2 M^{-1}.

[Pt(pap)(cat)] (3). Yield: 83 mg (0.17 mmol, ∼63%). Anal. Calcd for $C_{17}H_{13}N_3O_2Pt$ (M_w = 486.39): C, 41.98; H, 2.69; N, 8.64. Found: C, 41.68; H: 2.53; N, 8.72. ^{1}H NMR (400 MHz, $CDCl_3$): δ 9.48 (s, 1H, azo), 8.48 (d, 2H, J = 7.6 Hz, azo), 8.09 (s, 1H, azo), 7.95 (s, 1H, azo), 7.51 (d, 4H, J = 8 Hz, azo), 6.92 (d, 1H, J = 6.8 Hz, catechol), 6.86 (d, 1H, J = 7.2 Hz, catechol), 6.48 (t, 2H, J_1 = 5.2 Hz, J_2= 4.8 Hz, catechol). ^{13}C NMR (100 MHz, $CDCl_3$): δ 153.484, 147.835, 139.82, 133.65, 129.29, 127.57, 126.26, 124.60, 119.33, 118.26, 116.37, 116.06.^{195}Pt NMR (86 Hz, $CDCl_3$): δ −1544.4. ESI-MS (in MeCN): m/z 487.0720 ([M + H]$^+$, 100%). Calcd: m/z 487.0734. UV−visible in 10% DMSO/PBS (pH 7.2) [λ, nm (ε, M^{-1} cm^{-1})]: 760 (2660), 377 (7250), 288 (11650). Selected IR data (cm^{-1}): 1456 (s), 1250 (s), 770 (m), 530 (w). Molar conductance in DMF at 298 K (Λ_M): 34 S m^2 M^{-1}.

dx.doi.org/10.1021/ic502317z | *Inorg. Chem.* 2015, 54, 253−264

Solubility. The ligands and complexes were soluble in methanol, ethanol, acetonitrile, DMF, DMSO, dichloromethane, chloroform, and ethyl acetate.

X-ray Crystallographic Procedure. The crystal structure of **3** was obtained by a single-crystal X-ray diffraction method. Red rectangular block crystals of **3** were obtained upon slow evaporation of an acetonitrile/ethanol solution of the complex. The crystal was mounted on a loop with paratone oil. All geometric and intensity data were collected using an automated Bruker SMART APEX CCD diffractometer equipped with a fine focus 1.75 kW sealed-tube Mo Kα X-ray source (λ = 0.71073 Å) with increasing ω (width of 0.3° frame^{-1}) at a scan speed of 5 s frame^{-1}. Intensity data were collected using the ω−2θ scan mode and then corrected for Lorentz−polarization and absorption effects.[35] The structures were solved and refined using the *WinGx* suite of programs (version 1.63.04a) by the *SHELXL-2013* method.[36] The non-hydrogen atoms were refined with anisotropic displacement coefficients, and their coordinates were permitted to ride on their respective carbon atoms. Two Q peaks of 5.10 and 4.99 electron density were observed in the final difference Fourier map located at distances of 2.138 Å (molecule A) and 2.349 Å (molecule B) from two platinum centers. These peaks are ∼1.01 Å from the nearest oxygen atoms of two catecholate ligands. These peaks, which are possibly arising because of the presence of platinum as a heavy metal, did not affect the overall structure, and there was no major alert seen in the checkCIF/PLATON report. The perspective views of molecules A and B of complex **3** in the crystallographic asymmetric unit are represented using *ORTEP*.[37] Selected crystallographic data are given in Table 1. The CCDC deposition number is 1024788.

Table 1. Selected Crystallographic Data for Complex 3

empirical formula	$C_{17}H_{13}N_3O_2Pt$
fw/g M^{-1}	486.38
cryst syst	triclinic
space group	$P\bar{1}$
a/Å	7.6344(14)
b/Å	12.533(3)
c/Å	16.608(4)
α/deg	102.867(8)
β/deg	96.576(8)
γ/deg	104.568(8)
V/Å^3	1474.7(6)
Z	4
$2\theta_{max}$/°	50.5
T, K	293(2)
ρ_{calcd}/Mg m^{-3}	2.19
λ(Mo Kα)/Å	0.71073
μ/mm^{-1}	9.53
data/restraints/param	5256/0/415
F(000)	920
GOF	1.078
$R(F_o)$,[a] with $I > 2\sigma(I)$ [$R_w(F_o)$[b]]	0.0620 [0.1707]
R (all data) [R_w (all data)]	0.0884 [0.1802]
largest diff peak, hole (e Å^{-3})	5.096, −1.599

[a] $R = \sum||F_o| - |F_c||/\sum|F_o|$. [b] $R_w = \{\sum[w(F_o^2 - F_c^2)^2]/\sum[w(F_o)^2]\}^{1/2}$; $w = [\sigma^2(F_o)^2 + (0.0941P)^2 + 16.7435P]^{-1}$, where $P = (F_o^2 + 2F_c^2)/3$.

Cell Viability Assay. The cytotoxicity of the complexes was evaluated from a MTT, 3-(4,5-dimethylthiazol-2-yl)-2,5-diphenyltetrazolium bromide, assay. The formazan formed was dissolved in DMSO for quantification by a spectral method. The experimental details are given in the SI. Photoirradiation with visible light of 400−700 nm was done for 1 h using a Luzchem photoreactor (model LZC-1, Ontario, Canada; 10 J cm^{-2}). Experiments were also performed in red light of 600−720 nm (150 J cm^{-2}) using a Waldmann PDT 1200 L because the complexes had intense charge-transfer bands in the near-IR region.

2′,7′-Dichlorofluorescein Diacetate (DCFDA) Assay. DCFDA was used to detect the generation of any cellular reactive oxygen species (ROS). DCFDA upon oxidation by cellular ROS generates fluorescent DCF having an emission spectral maximum at 525 nm. The percentage of cell population generating ROS was determined by flow cytometry analysis. HaCaT and MCF-7 cells were incubated with complexes **1**−**3** for 4 h followed by irradiation with visible light of 400−700 nm for 1 h in DPBS. These cells were subsequently harvested by trypsinization, and a single cell suspension of ∼10^6 cells mL^{-1} was made. The cells were then treated with 1 μM DCFDA solution in DMSO in dark for ∼20 min at room temperature. The distribution of DCFDA-stained cells was determined by flow cytometry in the FL-1 channel.

Annexin V−Fluorescein Isothiocyanate (FITC)/Propidium Iodide (PI) Assay. HaCaT and MCF-7 cells (3×10^5) were plated in six-well plates and grown for 24 h. Cells were incubated with DMSO solutions [1% in Dulbecco's modified Eagle medium (DMEM)/10% fetal bovine serum (FBS)] of complexes **1**−**3** (along with untreated controls) for 4 h followed by photoexposure for 1 h (400−700 nm, 10 J cm^{-2}) in DPBS. After treatment, cells were allowed to grow for 12 h, washed twice in DPBS, and trypsinized. Cells were resuspended in 500 μL of a 1X binding buffer. Annexin V−FITC (2 μL) and PI (1 μL) were added to each cell suspension. Incubation at room temperature was done for 10 min in dark. The fluorescence of the cells was determined with a flow cytometer.

Cell Cycle Analysis. HaCaT and MCF-7 cells (∼3×10^6) were plated per well of a six-well tissue culture plate in DMEM containing 10% FBS. After 12 h of incubation at 37 °C in a CO_2 incubator, DMSO solutions (1% in DMEM/10% FBS) of complexes **1**−**3** were added to the cells, and incubation was continued in the dark for 4 h. The medium was subsequently replaced with DPBS, and photoirradiation was done for 1 h in light of 400−700 nm. After irradiation, cells were allowed to grow in the dark for a further period of 12 h and then trypsinized and centrifuged. The cells were washed once with chilled DPBS and fixed by the addition of 800 μL of chilled 70% ethanol dropwise with simultaneous pipetting to prevent any cell aggregation. The cell suspensions were incubated at −20 °C for 6 h. The fixed cells were then washed twice with 1 mL of chilled DPBS by centrifuging at 4000 rpm at 4 °C for 5 min. After the supernatants were discarded, the cell pellets were suspended for 12 h at 37 °C in 200 μL of DPBS-containing 10 μg mL^{-1} DNase-free RNase. After digestion of cellular RNA, a 20 μL volume of a 1 mg mL^{-1} PI solution was added to both mixtures and incubated at 25 °C in the dark for another 20 min. Flow cytometric analysis was performed using a FACS Calibur BD cell analyzer, at the FL2 channel (595 nm), and the distribution of cells in various cell cycle phases was determined from the histogram generated by *Cell Quest Pro* software (BD Biosciences). Data analysis was performed for the percentage of cells in each cell cycle phase by using *WinMDI*, version 2.8.

Fluorescence Microscopy. Fluorescence images of complexes **1** and **2** and ligands in HaCaT and MCF-7 cells were obtained using an Olympus 81X fluorescence microscope. Cells were grown at a seeding density of ∼5×10^4 cells in 1 mL of the culture medium for 24 h. They were treated with the complexes (15 μM) for 2 and 4 h in the dark, fixed, and permeabilized with chilled ethanol for 5 min at −20 °C. Ethanol was removed, and the cells were washed one time with PBS, incubated with PI (10 mg mL^{-1}, diluted to 1:4) to stain the nucleus for 2 min, and visualized under a microscope.

Cellular Uptake from Platinum Estimation. To quantify the total platinum uptake, about 10^6 HaCaT and MCF-7 cells were seeded in 60 mm tissue culture dishes. The detailed experimental procedure is given in the SI. The samples were run using ICP-MS for the platinum content along with the standards (0.01−1 ppm and a blank sample fitted in a linear plot with a correlation of 0.99). The platinum content obtained in ppb units was then expressed as pg/10^6 cells.

Theoretical Calculations. Calculations were done using the B3LYP functional using mixed basis sets [LanL2DZ (for the platinum atom)/6-31+G (for all other atoms)] with the *Gaussian 09* suite of

dx.doi.org/10.1021/ic502317z | *Inorg. Chem.* 2015, 54, 253−264

Table 2. Selected Physiochemical Data of Complexes 1−3 and Ligands H_2an-cat and H_2py-cat

data	complex 1	complex 2	complex 3	H_2an-cat	H_2py-cat
$\lambda_{max}{}^{a}$/nm (ε/ $M^{-1}cm^{-1}$)	800 (1663), 390 (7980)	788 (2000), 397 (10366)	761 (2658), 377 (7249)	389 (5391), 370 (5438)	390 (9325), 360 (20879)
$\lambda_{em}{}^{b}$/nm [Φ^{c}]	451, 426 [0.015]	440, 415, 390 [0.025]		445, 420, 398 [0.05]	415, 400 [0.06]
$\lambda_{em}{}^{d}$/nm [Φ^{c}]	505, 454, 425 [0.016]	470 [0.024]		505 [0.07]	470 [0.04]
$E_f{}^{e}$/V [ΔE_p/ mV]	1.12, 0.42 [360], −1.25, −0.34 [65]	1.13, 0.42 [360], −1.29, −0.33 [65]	0.65, 0.88, −1.24 [90], −0.33 [80]	0.57 [170], 0.45 [380]	1.15, 0.45 [440]
$\Lambda_M{}^{f}$/S m^2 mol^{-1}	34	40	34		
$K_b{}^{g}/M^{-1}$	0.20 (±0.03) × 10^5	0.30 (±0.05) × 10^6	0.50 (±0.02) × 10^3	0.70 (±0.03) × 10^5	0.50 (±0.03) × 10^6
$\Delta T_m{}^{h}$/°C	3.3	5.3	2.1	5.6	7.7

[a]In 10% DMSO/DPBS (pH 7.2). [b]Emission spectra in DMSO (λ_{ex} = 370 nm). [c]The quantum yield is measured by taking pure anthracene in ethanol (Φ = 0.27) as the standard. [d]Emission spectra in 99.5% PBS/DMSO (λ_{ex} = 370 nm). Errors for quantum yield measurements are within ±10%. [e]Peaks corresponding to cyclic voltammograms of a 1 mM sample in DMF/0.1 M TBAP. $E_f = 0.5(E_{pa} + E_{pc})$. $\Delta E_p = (E_{pa} - E_{pc})$, where E_{pa} and E_{pc} are the anodic and cathodic peak potentials, respectively. The potentials are versus SCE (E_0 = 0.244 V). Scan rate = 100 mV s^{-1}. [f]Molar conductivity in DMF. [g]Intrinsic equilibrium ct-DNA binding constant (K_b) from UV−visible absorption spectral experiments. [h]Change in the ct-DNA melting temperature upon the addition of the complexes and ligands (ethidium bromide as a reference showing ΔT_m = 13 °C).

programs.[38,39] The electronic transitions along with the oscillator strengths were evaluated using linear-response time-dependent density functional theory (TDDFT).[40]

DNA Binding Experiments. Absorption titration experiments were performed in a Tris-HCl buffer (5 mM, pH 7.2) by varying the concentration of calf thymus (ct)-DNA (stock concentration of 210 μM) while keeping the complex concentration constant (50 μM in DMF). The intrinsic equilibrium binding constants (K_b) of complexes to ct-DNA were obtained by the McGhee−von Hippel method using the expression of Bard and co-workers by regression analysis.[41,42]The DNA thermal denaturation experiments were done by measuring the absorption intensity of ct-DNA (200 μM) at 260 nm at elevated temperatures (from 40 to 90 °C), in both the absence and presence of complexes **1**−**3** (20 μM) and ligands (20 μM). The viscometric titrations were performed to determine the relative specific viscosity of the ct-DNA solution (170 μM) in a 5 mM Tris-HCl buffer in the presence of complexes **1**−**3** and free ligands. The relative specific viscosity of DNA, $(\eta/\eta_0)^{1/3}$, was plotted against [complex]/[DNA], where η and η_0 are the viscosity of DNA in the presence and absence of the complex.

DNA Photocleavage Experiments. The cleavage of SC pUC19 DNA (0.2 μg, 30 μM, 2686 base pairs) in the presence of complexes **1**−**3** (40 μM in DMF) was determined by agarose gel electrophoresis using the complexes in a 50 mM Tris-HCl buffer (pH 7.2) and 50 mM NaCl containing 10% DMF. The photoinduced DNA cleavage reactions were done using a diode laser of 785 nm wavelength (LQC705-38E, Newport Corp.; power 40 mW). Before light exposure, each sample was incubated for 1 h at 37 °C and analyzed for photocleaved products by the gel electrophoresis method. Mechanistic investigations were done by adding different additives as ROS scavengers/quenchers (NaN_3, 4 mM; TEMP, 4 mM; DABCO, 4 mM; DMSO, 8 μL; KI, 4 mM; catalase, 4 units; SOD, 4 units, 10 mM GSH).

3. RESULTS AND DISCUSSION

Synthesis and General Aspects. The catecholate derivatives were prepared using dopamine hydrochloride and 9-anthracene carboxaldehyde for H_2an-cat or 1-pyrene carboxaldehyde for H_2py-cat. The complexes were prepared in good yield (∼75%) from the reaction of [Pt(pap)Cl_2] and the ligand (H_2an-cat for **1**, H_2py-cat for **2**, and H_2cat for **3**) in methanol in the presence of triethylamine under a nitrogen atmosphere and ambient conditions (Scheme S2 in the SI). The complexes showed a single HPLC-MS peak in the chromatograms, confirming their purity (Figure S7 in the SI). The complexes were characterized from their physicochemical data (Table 2). The mass spectra in acetonitrile showed a single peak (m/z 718.20 for **1**, m/z 742.17 for **2**, and m/z 487.07 for **3**) corresponding to the ionized form with an isotopic distribution pattern for platinum in the fragments indicating the stability of the complexes under applied voltages (Figures S8−S10 in the SI). The ^{1}H NMR spectra of the ligands showed a characteristic singlet peak at 9.2 ppm, which is assignable to the hydrogen atom of the imine bond (Figure S1 in the SI). The aromatic hydrogen atom peaks of the anthracenyl or pyrenyl moiety lie in the range of 7.0−9.3 ppm, while three hydrogen atoms of the catechol ring gave signals near 6−7 ppm. Two additional peaks observed at 2.9 and 4.1 ppm are assignable to the hydrogen atoms of the methylene groups. The ^{13}C NMR spectra of the ligands also showed the presence of an imine carbon, giving a signal at 161 ppm (Figure S2 in the SI). Two carbon atoms containing the OH moiety appeared at 144 and 146 ppm. The signals at 37 and 64 ppm were assignable to the methylene carbon atoms. The ^{1}H and ^{13}C NMR spectra of the complexes showed peaks similar to those observed for the free ligands (Figures S11−S13 in the SI). Some additional peaks in the aromatic region were noted in the spectra of the complexes, which are due to the hydrogen and carbon atoms of the pap ligand. The ^{195}Pt NMR spectrum of complex **3** displayed a peak at −1544.4 ppm in $CDCl_3$.

The IR spectra of the complexes showed the disappearance of the sharp signal of the O−H stretching frequency around 3400−3500 cm^{-1}, present in the free ligands, indicating the loss of hydroxyl hydrogen upon binding to the metal ion, with the appearance of a weak signal near 550 cm^{-1} assignable to the Pt−O bond (Figure S14 in the SI). Two intense signals within 1605−1610 and 1250−1270 cm^{-1} are the C═N and C−N stretching frequencies, respectively. The complexes gave conductance values of ∼35 S m^2 M^{-1} at 25 °C in DMF, indicating the nonconducting nature of the complexes.[43] The complexes showed four cyclic voltammetric responses in DMF/0.1 M TBAP (Figure S15 in the SI). The responses near 1.0 and 0.4 V are attributed to two one-electron-oxidation processes involving the catecholate moiety. The anodic redox responses vary from quasi-reversible to irreversible in nature, depending upon the substituent present at the para position of the catecholate ring. The responses at −0.3 and −1.3 V are due to two-step azo reductions, resulting in the formation of monoanionic and dianionic radical pap species.[44,45] There is a positive shift of the pap reduction potential upon binding to the metal, making the complexes susceptible to reduction by biological entities like GSH in a cellular medium.

dx.doi.org/10.1021/ic502317z | Inorg. Chem. 2015, 54, 253−264

The UV−visible spectra of the complexes in 10% DMSO/PBS (pH 7.2) showed an intense but broad absorption band in the near-IR region with a maximum at ∼750 nm having a ε value of ∼2500 M^{-1} cm^{-1} (Figure 1a). This band is assignable

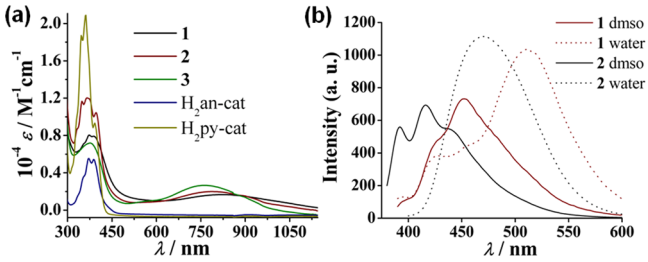

Figure 1. (a) UV−visible spectra of **1**−**3** and the ligands in 10% DMSO/PBS (pH 7.2). (b) Emission spectra of **1** and **2** in DMSO and in 99.5% aqueous DMSO (λ_{ex} = 370 nm).

to charge transfer involving the coordinated catecholate ligand and the 2-(phenylazo)pyridyl moiety. Additional peaks at 390 and 288 nm are due to ligand-centered transitions, mainly arising from the anthracenyl and pyrenyl moieties in complexes **1** and **2**, respectively. The emission spectra of the complexes and ligands were recorded at room temperature in DMSO and 99.5% aqueous DMSO solutions (Figures 1b and S16 in the SI). Complex **1** showed an emission band near 450 nm, while the same for ligand H_2an-cat was near 445 nm, which is characteristic of the anthracene fluorophore. Similarly, complex **2** showed an emission band around 440 nm, while the H_2py-cat ligand showed the same at 415 nm, fingerprinting the presence of a pyrenyl moiety. Upon dilution with water, the spectra were found to be red-shifted with an enhancement in the emission intensity. For complex **1** and H_2an-cat, the addition of water to DMSO solutions shifts the emission band with gradual broadening, attaining a maximum at 505 nm. A similar effect was observed for complex **2** and ligand H_2py-cat, with the band shifting to 470 nm. The shift was possibly due to aggregation-induced emission, which is reported to occur for the catechol-based ligands.[46−48] The pyrene-based complex **2** showed a quantum yield (Φ) value of 0.025, which is higher than that of the anthracenyl analogue **1** (Φ = 0.015).

Crystal Structure. Complex **3** was structurally characterized by an X-ray diffraction method. The complex crystallized in the triclinic space group $P\bar{1}$ with four molecules in the unit cell and two molecules in the crystallographic asymmetric unit. An ORTEP view of the complex (molecules A and B) is shown in Figure 2, and selected bond distances and angles are given in Table 3 (unit cell packing diagram in Figure S17 in the SI). The pendant phenyl rings of the pap ligands in molecules A and B are involved in chemically significant $\pi-\pi$-stacking interactions, thus giving two pairs of molecules in the unit cell with a Z value of 4. The structure shows a four-coordinate planar geometry of platinum(II), with pap and cat showing bidentate chelating modes of bonding. The N1−N2 (molecule A) and N4−N5 (molecule B) bond lengths of 1.310(19) and 1.286(13) Å are typical for azo double bonds with nitrogen atoms coordinated to the platinum center.[49] The π-back-donation from platinum has resulted in an increase in the bond length by 0.5 Å compared to the typical azo bond lengths in an uncoordinated pap ligand.[50] Similarly, the N1−C6 distance of 1.43(2) Å in molecule A [N4−C23 distance of 1.42(2) Å in molecule B] is longer than the N3−C1 distance of 1.36(2) Å [N5−C22

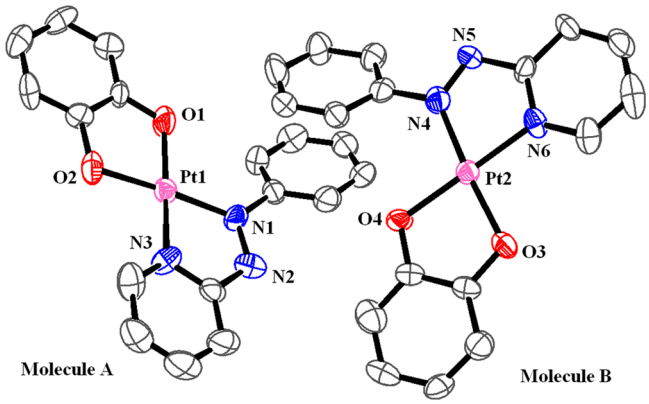

Figure 2. ORTEP views of complex **3** (molecules A and B) showing atom numbering schemes for the metal and heteroatoms. The thermal ellipsoids are at the 50% probability level. The hydrogen atoms are omitted for clarity. Color codes: platinum, light pink; nitrogen, blue; oxygen, red; carbon, gray.

Table 3. Selected Bond Lengths (Å) and Angles (deg) of 3 with Estimated Standard Deviations in Parentheses

	complex **3**	
	molecule A	molecule B
Pt1−N1	1.956(13)	
Pt1−N3	1.959(13)	
Pt2−N4		1.938(14)
Pt2−N6		1.976(12)
Pt1−O1	1.975(13)	
Pt1−O2	1.976(12)	
Pt2−O3		1.977(12)
Pt2−O4		1.989(10)
N1−N2	1.310(19)	
N4−N5		1.286(18)
N1−C6	1.43(2)	
N2−C1	1.36(2)	
N4−C23		1.42(2)
N5−C22		1.396(19)
N1−Pt1−N3	79.9(6)	
N1−Pt1−O1	101.2(5)	
N3−Pt1−O2	94.8(6)	
O1−Pt1−O2	84.1(5)	
N4−Pt2−N6		78.2(5)
N4−Pt2−O4		100.6(5)
N6−Pt2−O3		97.6(5)
O3−Pt2−O4		83.6(4)

distance of 1.396(19) Å in molecule B]. The Pt−N and Pt−O bonds are ∼1.9 Å.

Photocytotoxicity. The cytotoxicity of the complexes was assessed by MTT assay using two human cell lines, viz., skin keratinocytes HaCaT and breast cancer MCF-7cells, with two preincubation time periods of 4 and 24 h. The growth inhibition values (IC_{50} values) were determined both in the dark and after photoexposure with visible light of 400−700 nm (10 J cm^{-2}; Figures 3 and S18−S20 in the SI). A comparison of the IC_{50} values of the complexes and a few platinum(II) complexes has been made in Table 4.[51,52] The ligands H_2an-cat and H_2py-cat as photosensitizers show photocytotoxicity in visible light giving IC_{50} values of ∼9.0 μM in HaCaT and ∼10 μM in MCF-7. Complex **1** showed a significant enhancement in

dx.doi.org/10.1021/ic502317z | Inorg. Chem. 2015, 54, 253−264

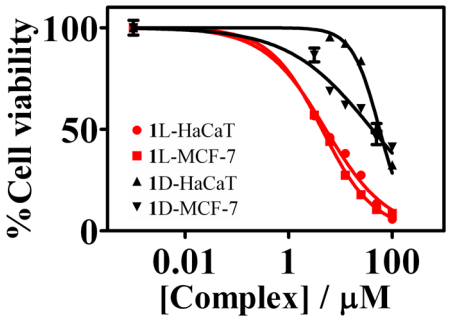

Figure 3. Cell viability plots from MTT assay of complex **1** showing cytotoxicity in HaCaT and MCF-7 cells (4 h of preincubation) in visible light (400−700 nm, red symbols) and the dark (black symbols).

the cytotoxicity, as can be seen from the IC_{50} values upon photoirradiation in both cells, thus exemplifying it as a potent PDT agent. The IC_{50} value of <5.2 μM of **1** in light is comparable to that of cisplatin in the dark upon 24 h incubation. Complex **2** gave IC_{50} values of 19.6 and 14.1 μM in HaCaT and MCF-7 cells in light. Though pyrene is a better photosensitizer than anthracene, complex **2** showed a lower PDT effect than **1** possibly because of the formation of aggregates in solution, as evidenced from the emissive properties of the complexes. Aggregate formation substantially quenches the triplet state and reduces the generation of ROS, thus resulting in reduced photoactivity. It is well documented that planar extended aromatic moieties like phthalocyanines, porphyrins, and pyrenes exhibit potent photosensitizing abilities only in monomeric species and also, to some extent, in planar end-to-end aggregates.[53,54] Control complex **3**, which lacks any photosensitizer, gave similar IC_{50} values in both the dark and light (~20 μM for HaCaT and 12 μM for MCF-7) and exhibited no apparent PDT effect in both cell lines. Preincubation of the cells with the complexes for 24 h resulted in higher dark toxicity of the complexes and no significant difference between the IC_{50} values in the dark and light. The observed photocytotoxicity by the anthracene- or pyrene-appended catecholate complexes has led us to carry out further bioexperiments with a 4 h preincubation time period in both the dark and light (400−700 nm; 10 J cm^{-2}) to investigate other cellular properties of the complexes. We also studied the photocytotoxicity in red light of 600−720 nm (150 J cm^{-2}) using a photoreactor (Waldmann PDT 1200 L). The complexes, however, did not show any enhanced cytotoxicity in red light.

Annexin V−FITC/PI Assay. The mode of cellular death was studied by annexin V−FITC/PI assay in both HaCaT and MCF-7 cell lines using flow cytometry. This assay was used to differentiate dead, late apoptotic, and early apoptotic cells on the basis of the different permeabilities of the dyes used.[55] Live cells are impermeable to both dyes (LL quadrant). The dead cells uptake PI (UL quadrant), the late apoptotic cells uptake both PI and annexin V−FITC (UR quadrant), and the early apoptotic cells uptake only the annexin V−FITC dye (LR quadrant). The HaCaT and MCF-7 cells were treated with the complexes (concentration corresponding to the respective IC_{50} value in light) for 4 h, followed by 1 h of photoirradiation with visible light (400−700 nm). FACS readings were taken after postprocessing of the treated cells. On the basis of the cell populations in the different quadrants, the potency of the complex was evaluated for early/late apoptosis. From the dot plots shown in Figure4 (Figures S21−S24 in the SI), it is apparent that complex **1** exhibited maximum apoptosis in both cell lines upon photoirradiation. Complex **1** in HaCaT cells induced early apoptosis upon light exposure, showing an increase of ~11% cell population in the LR quadrant, while in MCF-7 cells, it triggers both early and late apoptosis, as indicated by almost a ~40% increase in the cell population in the LR and UR quadrants upon photoirradiation. Complex **2** showed an increase in the apoptotic cell population of 4% upon light irradiation. In contrast, complex **3** resulted in almost equal apoptotic cell death (10%) in dark and light conditions in both cell lines.

Cell Cycle Analysis. The effect of the complexes on cell cycle progression was investigated in both HaCaT and MCF-7 cells upon 4 h of incubation in the dark and followed by 1 h of light (400−700 nm) exposure. Different phases of the cell cycle could be distinguished from the fluorescence intensity of PI. The basic principle of this method is that the DNA content of the cells duplicates during the S phase, thereby giving almost double the fluorescence intensity in the G2/M phase than in

Table 4. Photocytotoxicity of Complexes 1−3 and Related Compounds

	HaCaT		MCF-7	
complex	IC_{50}[a](light) (μM)	IC_{50}[b](dark) (μM)	IC_{50}[a](light) (μM)	IC_{50}[b](dark) (μM)
1	5.2 ± 0.1	57.0 ± 1.2	4.4 ± 0.2	43.5 ± 0.8
2	19.6 ± 0.7	>50	14.1 ± 0.2	27.8 ± 0.2
3	17.6 ± 0.2	18.4 ± 0.4	11.1 ± 0.1	13.5 ± 0.2
H_2an-cat	9.6 ± 0.1	>50	7.5 ± 0.2	>50
H_2py-cat	9.2 ± 0.1	>50	11.7 ± 0.1	>50
pap	>50	>50	>50	>50
cisplatin[c]		3.2 ± 0.3		69.7 ± 1.2
[Pt(Fc-tpy)Cl]Cl[c]	12.0 ± 0.2	68.4 ± 0.3	12.2 ± 0.5	74.8 ± 1.1
[Pt(pyddpz)(C≡CFc)]Cl[d]			6.5 ± 0.1	>25
$[Pt(NHC)_2]OTf$[e]			7.25 ± 0.99	152.6 ± 23.9
platinum(IV) azide[f]	6.1 (5.6−6.6)	>244.3		

[a]The IC_{50} values (μM) in HaCaT and MCF-7 cells exposed to 4 h of incubation with complexes in the dark, followed by 1 h of irradiation (400−700 nm; 10 J cm^{-2}). [b]The IC_{50} values in HaCaT and MCF-7 cells treated with the complexes and incubated for 4 h in the dark. [c]The IC_{50} values upon 24 h of incubation taken from ref 25. The ligand is ferrocenyl-appended terpyridine. [d]The IC_{50} value data as given in ref 24. The pydppz ligand is pyridyldipyridophenazine. [e]The data for organometallic platinum(II) N-heterocyclic carbene (NHC) complexes showing phototoxicity in visible light (2.8 mW cm^{-2}) taken from ref 51. [f]The data for a platinum(IV) azide complex showing cytotoxicity in UVA light (365 nm) taken from ref 52.

dx.doi.org/10.1021/ic502317z | Inorg. Chem. 2015, 54, 253−264

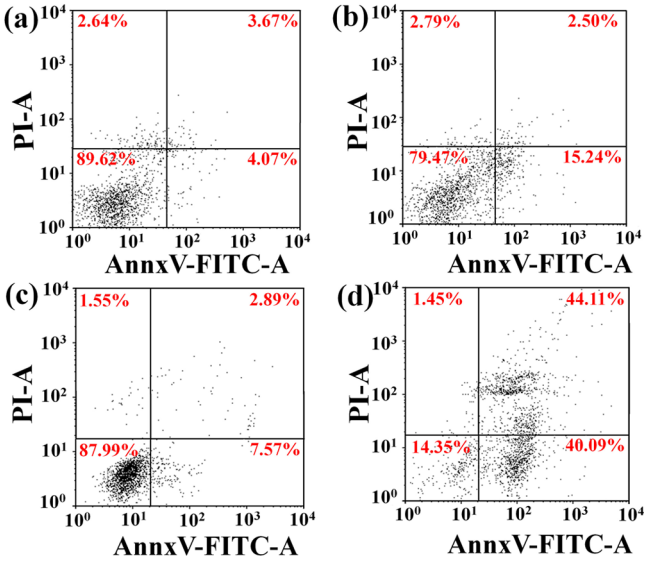

Figure 4. Dot plots of annexin V−FITC/PI assay on HaCaT (a and b) and MCF-7 (c and d) cells treated for 4 h with complex **1** (10 μM) in the dark (a and c) and irradiated with visible light (400−700 nm) for 1 h (b and d). % Ccell populations in the respective quadrants are shown: lower left (LL), live cells; lower right (LR), early apoptotic; upper left (UL), dead cells; upper right (UR), late apoptotic.

the G0/G1 phase. From the histograms, the populations in the different phases of the cell cycle are obtained and given as a bar diagram in Figure 5a (Figures S25 and S26 in the SI). Complex

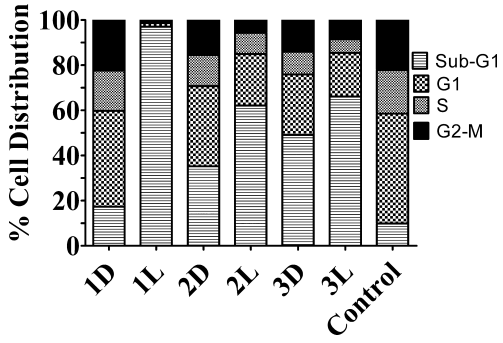

Figure 5. Bar diagram showing % HaCaT cell populations upon treatment with **1** (10 μM), **2** (20 μM), and **3** (10 μM) in light (L) and the dark (D) in various phases of the cell cycle.

1 showed an increase of ∼80% in the sub-G1 population in HaCaT cells upon light exposure, which is in agreement with the greater potency to cause photoinduced apoptosis as observed from the annexin V−FITC/PI assay. Complex **2** showed a ∼40% increase in the sub-G1 population in light-exposed HaCaT cells, while complex **3** displayed ∼50% of the sub-G1 population in HaCaT cells treated under light or dark conditions. The complexes showed a similar cell cycle arrest in MCF-7 cells.

Generation of ROS. The involvement of any ROS in the photocytotoxic reactions was investigated from DCFDA assay using both HaCaT and MCF-7 cells. DCFDA upon oxidation by ROS generates green fluorescent DCF, which can be readily detected.[56] The shift in the band position can be correlated with the amount of ROS generated within the cell. Complexes **1** and **2** showed the formation of ROS upon light exposure in the cells, as indicated by the shift in the band position of the spectra shown in Figure 6 (Figures S27 and S28 in the SI). In contrast, complex **3** did not show any shift in the band position

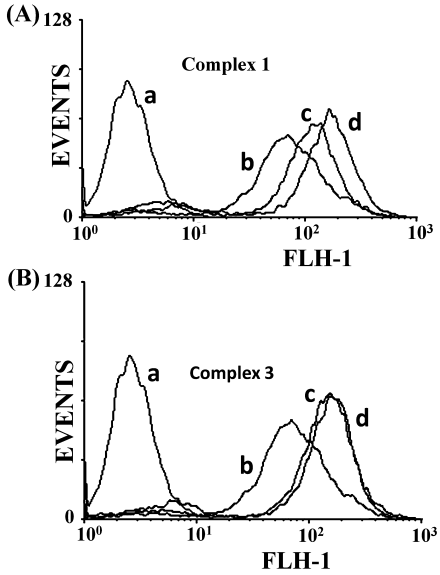

Figure 6. DCFDA assay on HaCaT cells treated with 10 μM of **1** (A) and **3** (B) for 4 h and irradiated in visible light (400−700 nm) for 1 h [a, cells alone; b, cells + DCFDA; c, cells + DCFDA + complex (dark); d, cells + DCFDA + complex (light)].

upon exposure to light, suggesting no enhancement of ROS production upon light exposure (Figure S28 in the SI). This is consistent with the data showing the photoinactive nature of complex **3**.

Stability of the Complexes. The cellular data suggest that the photocytotoxic action of the complexes is due to the generation of ROS, which promoted cellular death via apoptosis. However, the reason for any dark toxicity and the inability of the complexes to show any enhanced phototoxicity in red light is unclear. Cisplatin and its analogues, viz., carboplatin, oxaliplatin, etc., are the anticancer drugs showing cytotoxicity by slow hydrolysis within the cell and the release of (ammine)(aqua)platinum(II) complexes capable of binding to DNA and triggering cellular apoptosis.[4,5] Similarly, the release of the O^O donor catecholate from the present complexes could result in the formation of a pap-coordinated platinum(II) moiety, which can behave like hydrolyzed cisplatin species with an ability to covalently bind the DNA nucleobases. To probe this aspect, we studied the stability of the complexes in the presence or absence of various cellular analytes in 10% DMSO/PBS (pH 7.2) in dark reaction conditions. The strong absorption band in the near-IR region was the signature of coordination of the catechol ligand with the pap-bound platinum(II) center, and its intensity was used to follow the kinetics. Complexes **1**−**3** were found to be almost inert toward hydrolysis, which was evident from the very gradual decrease of the intense broad band around 700−750 nm even after 24 h of incubation (Figure S29 in the SI). The respective initial rates of hydrolysis [k_{hyd}] for complexes **1**−**3**(100 μM) were found to be 1.24×10^{-8}, 1.48×10^{-8}, and 1.18×10^{-8} M min^{-1} (errors within ±5%).

To ascertain the ability of the complexes to form Pt-GMP adducts, complexes **1**−**3** (100 μM) were treated with 5′-GMP (guanosine monophospate). The UV−visible spectra of the complexes in the presence of excess 5′-GMP in the molar ratio

dx.doi.org/10.1021/ic502317z | Inorg. Chem. 2015, 54, 253−264

of 1:10 did not show any appreciable change over 48 h, and no new peaks appeared (Figure S30 in the SI). The ^{1}H NMR spectral data of complex **3** (500 μM) recorded in a 3:1 D_2O/MeOD-d_4 solvent in the presence of excess 5′-GMP (5 mM) also indicated no adduct formation with 5′-GMP (Figure S31 in the SI). There was no upfield shift of the N-7 proton even after 48 h of incubation at room temperature, indicating no coordination of platinum species to the nitrogen of 5′-GMP. The low hydrolysis rate and inability to bind to DNA bases could not account for the observed significant dark toxicity exhibited by the complexes. This led us to investigate the additional factors contributing to the antiproliferative properties of the complexes. The cyclic voltammetric data suggested that the azo bond present in the complexes is susceptible to reduction. Cellular reducing agents such as tripeptide GSH are often overexpressed in tumors (intercellular concentration > 10 mM), and GSH could possibly interact with the complexes.[57] It was observed that, in the presence of excess GSH (500 μM), the green color of the complex solutions (100 μM) gradually changed to purple, then brown, and finally black. Upon monitoring of the UV−visible spectra in 10% DMSO/phosphate buffer (pH 7.2), a gradual decrease in the intensity of the absorption band was observed at 700−750 nm, indicating the probable loss of the catecholate ligand and a concomitant appearance of two new peaks at 599 and 520 nm (Figure S32 in the SI). Interestingly, similar peaks at 599 and 520 nm appeared when the precursor complex [Pt(pap)Cl_2] was treated with excess GSH (Figure S32 in the SI). These peaks arise probably because of the intraligand charge-transfer (ILCT) transitions in the pap radical anion and metal-to-ligand charge-transfer transitions. The observations were in accordance with the literature reports of reduction of the azo-bound ruthenium arene complexes by GSH.[30−32] The respective initial rates (k_{GSH}) of complexes **1**−**3** were 8.18×10^{-7}, 8.10×10^{-7}, and 8.86×10^{-7} M min^{-1} (errors within ±10%). Complex **3** reacted comparatively faster with GSH, suggesting that the nature of the substituent at the para position in the catechol ring alters the reaction rates, which can also be correlated with the varying reduction potentials in the observed cyclic voltammetric responses. When the complex/GSH ratio is altered, it was observed that the initial rate increases with an increase in the concentration of GSH (Figure S33 in the SI). The reduction process was also confirmed by NMR spectroscopy, where the splitting of the β-CH_2 proton peaks of GSH at 2.92 and 3.15 ppm was found upon treatment with the complexes, which is possibly due to the formation of glutathione disulfide (GSSG; Figure S34 in the SI). Upon incubation of the complexes (500 μM) with excess GSH (5 mM) for 24 h, new peaks at 2.98, 2.82, and 3.12 ppm were found to appear, which can be assigned to β-CH_2 of GSSG. No such peaks were found when GSH alone was kept for 24 h under similar experimental conditions (Figure S34 in the SI).

Mass spectral studies of these samples gave additional support in which peaks corresponding to both GSSG {m/z 613.15 [(GSSG + H)$^+$] and 635.14 [(GSSG + Na)$^+$]} and free ligands {m/z 366 [(H_2py-cat + H)$^+$] and 242 [(2H_2cat + Na)$^+$]} were observed (Figure S35 in the SI). Further confirmation was obtained from the HPLC chromatograms, which clearly indicated the loss of ligands from the complexes upon incubation with excess GSH for 5 h (Figure S36 in the SI). The free ligands have higher emission intensity compared to the one coordinated to the metal center because of partial quenching. Therefore, release of free ligand from the complex can be easily registered by monitoring the emission intensity. The fluorescence intensity of complexes **1** and **2** when treated with 10 equiv of GSH was found to increase, indicating loss of the catecholate ligand (Figure S37 in the SI). Control experiments with only the complexes resulted in no change in the emission intensity over a period of 24 h. This experimental fact also favored our argument of the release of the catecholate in the presence of GSH. Thiols generally have a strong affinity to bind to the platinum moiety, which may result in reduced pap-coordinated Pt-GSH adducts.[58] The mass spectra of isolated fractions from the HPLC chromatogram showed a peak that was assigned to the reduced pap Pt-GSH biadduct (m/z 989.1896; Figure S38 in the SI). All of the above experimental data suggest that the complexes undergo both substitution and reduction reactions in the presence of GSH. However, the pap ligand alone as a control did not show any reduction in the presence of GSH, indicating the necessity of coordination to a metal center in order to shift the reduction potential to biologically accessible values.

Apart from GSH, there are other reducing and chelating biomolecules such as ascorbic acid and L-methionine in the cellular environment, and we studied their effects on the complexes as well. The complexes were treated with excess ascorbic acid, which is a mild reducing agent, and L-methionine as a nonreducing chelating thiol. In both cases, the UV−visible absorption spectra showed very slow decay of the intensity of the 700−750 nm band and the initial rates (k_{asc} and k_{met}) were found to be almost similar to that of the complexes alone in the aqueous media (Figure S39 and Table S2 in the SI). Mass spectral measurements of samples treated with an excess of the analytes after 48 h of incubation showed the formation of platinum adducts (Figure S40 in the SI). Upon a comparison of the initial rates of reaction with different additives, the trend was found to be $k_{GSH} \gg k_{asc} > k_{met} > k_{hyd}$. GSH functioning as both a powerful reducing agent and a better S-donor chelating ligand triggered faster loss of the ligand than either ascorbic acid (a weak O,O-donor ligand and mild reducing agent) and L-methionine (nonreducing S-donor ligand), and thus it can be inferred that the release is selectively triggered by GSH. Furthermore, the complexes are capable of reacting with DNA nucleobases within the cell upon cellular reduction by GSH and simultaneously releasing a photosensitizer bearing the catechol moiety, which can exert the PDT effect. These experimental findings validate the cytotoxic nature of the complexes in the dark, which possibly leads to both ROS generation due to redox instability and release of cytotoxins within the cell. This also explained why the complexes were noncytotoxic in red light. The complexes and free ligands were found to be photostable, showing no apparent change in the UV−visible spectra upon irradiation with visible light (400−700) nm for 1 h (Figure S41 in the SI).

Theoretical Study. Theoretical calculations were performed to understand the photophysical properties of the complexes. TDDFT studies were done to ascertain the origin of the intense broad band at 700−800 nm in the complexes and also the nature of the frontier orbitals. The geometries of the complexes with basic coordinates adapted from the crystal structure of **3** and modified as per requirements to develop the structures of **1** and **2** were initially optimized using the mixed basis sets B3LYP/LanL2DZ (for the platinum atom) and 6-31+G (for the rest of the atoms) (Figure S42 in the SI).[38−40] The energy-minimized coordinates of the complexes are listed in Table S3 (see the SI). The optimized geometries were used

dx.doi.org/10.1021/ic502317z | Inorg. Chem. 2015, 54, 253−264

to carry out the TDDFT calculations, employing the same level of theory. The probable transitions in the visible region and the nature of such transitions are listed in Table S4 (see the SI). The intense absorption band at the near-IR position for **1**−**3** was found to be a charge-transfer band arising from the transition from the catecholate moiety to the platinum-coordinated 2-(phenylazo)pyridyl moiety having high oscillator strength (f) values in the range 0.2−0.01. The theoretical data suggest that the experimentally observed decrease in the absorption intensity of such bands is due to loss of the catecholate ligand. The major transition (ligand-to-metal charge-transfer, LMCT) for complex **1** was found at ∼900 nm (f = 0.2). The other strong absorption was found at 413 nm (f = 0.13). This was found to be an ILCT band arising from transitions involving the anthracenyl moiety. Similarly for complex **2**, the LMCT band was found at 914 nm. The higher value of the oscillator strength of 0.2 indicated a higher probability of such transitions. The other strong absorption band was found at 400 nm with f = 0.27 involving ILCT transitions from the pyrenyl moeity. For complex **3**, the weak absorption at 417 nm was due to ligand-to-ligand charge-transfer and ILCT bands involving the metal-coordinated pap and catecholate moieties. The highest occupied molecular orbital (HOMO) for all complexes comprised orbitals of the catecholate moiety, while the lowest unoccupied molecular orbital (LUMO) was centered on the pap ligand (Figures 7 and

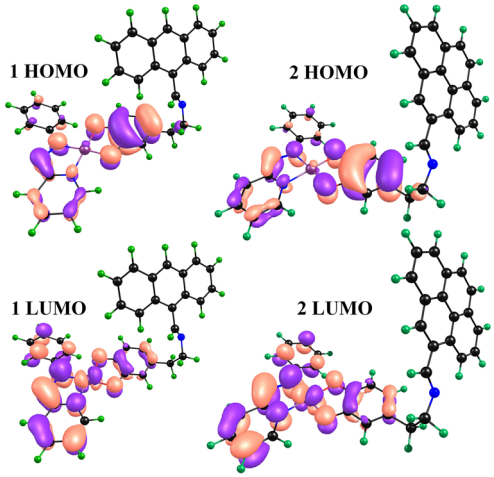

Figure 7. Frontier molecular orbitals of complexes **1** and **2** at a countervalue of 0.03. Theoretical calculations were done with B3LYP/LanL2DZ (for the platinum atom) and 6-31+G (for all other atoms) basis sets. Color code: platinum, magenta; nitrogen, blue; oxygen, red; carbon, black; hydrogen, green.

S42 in the SI). The frontier orbitals were of dissociative nature, indicating that reduction of the azo bond could lead to Pt−O bond dissociation. The HOMO−LUMO energy gap (ΔE) for complexes **1**−**3** are 1.407, 1.406, and 1.448 eV, respectively.

Fluorescence Microscopy. Complexes **1** and **2** and the catecholate derivatives were found to be emissive in the blue region because of the presence of the anthracenyl and pyrenyl fluorophores. In a typical experiment, HaCaT and MCF-7 cells were treated with 15 μM of the complexes or catecholate derivatives, and images were captured after 2 and 4 h of incubation (Figures 8 and S43 in the SI). PI was used as a nuclear staining dye. When the fluorescence microscopic images of the complexes were merged with that of PI, it was

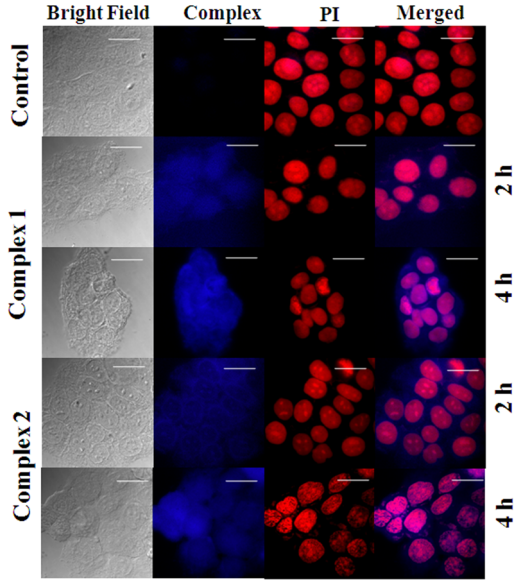

Figure 8. Fluorescence microscopic image of the complexes (20 μM) in HaCaT cells upon 2 and 4 h of incubation. The top row is for cells treated with only PI. The second and third rows are for **1**, while the fourth and fifth rows are for **2**. Scale bar = 10 μm. Substantial nuclear colocalization is seen upon 4 h of treatment in the merged images.

observed that both **1** and **2** preferentially colocalize in the nucleus. The free ligands (H_2an-cat and H_2py-cat) also showed preferential nuclear colocalization in both the HaCaT and MCF-7 cells (Figure S44 in the SI).

Cellular Platinum Content. Because both the complexes and ligands showed substantial nuclear localization, we carried out the estimation of platinum in the whole cell and also in the isolated nuclear and cytosolic fractions. Both HaCaT and MCF-7 cells were treated with complexes **1**−**3** (50 μM) for 3 h of preincubation, and the uptake was checked at two time points (3 and 6 h; Figure 9a). We observed that the total cellular uptake of complexes **1** and **2** (∼780 pg/10^6 cells) is higher than that of **3** (∼350 pg/10^6 cells) in HaCaT cells. This reflects the ability of the appended hydrophobic segments (anthracenyl and pyrenyl moieties) to facilitate uptake through the cytoplasmic membrane. However, no abrupt difference in the whole cell platinum content for **1** and **2** indicated that aggregation in the biological medium is more important than cellular uptake in governing the photocytotoxic behavior of the planar platinum(II) complexes. At the 6 h time point, we found an enhanced amount of platinum in the nuclear fraction for **1** and **2** (∼330 pg/10^6 cells) compared to the cytosolic fraction (∼220 pg/10^6 cells), and the nuclear platinum content increased with time (∼80 pg/10^6 cells). However, for complex **3**, the cytosolic and nuclear distribution patterns did not show any appreciable change in 3 and 6 h. The complexes showed similar uptake values in MCF-7 cells (Figure S45 in the SI).

DNA Binding Properties. The fluorescence microscopic images and cellular uptake data suggested localization of the complexes within the nucleus. The spectroscopic evidence also indicated GSH-mediated loss of the catecholate ligands. This has prompted us to study the DNA binding properties of the complexes by absorption, thermal denaturation, and viscometric methods. The equilibrium binding constant (K_b) values were obtained by the UV−visible spectral method using a complex solution of 50 μM and ct-DNA of 210 μM (Table 2 and Figure S46 in the SI). The K_b values varied as **2** > **1** ≫ **3**.

dx.doi.org/10.1021/ic502317z | Inorg. Chem. 2015, 54, 253−264

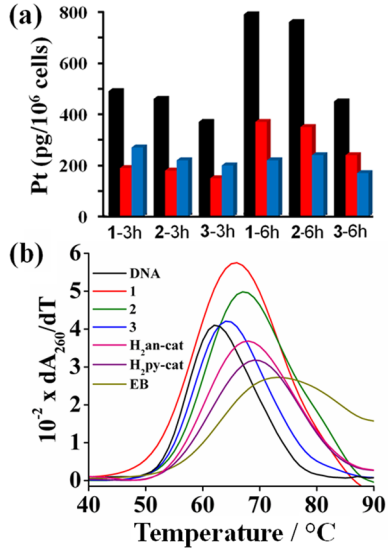

Figure 9. (a) Cellular uptake of complexes **1**−**3** in HaCaT cells at 3 and 6 h time points expressed as picograms of platinum per 10^6 cells. Whole cell, nuclear fractions, and cytosolic fractions are indicated by black, red, and blue bars, respectively. (b) Thermal denaturation plots of ct-DNA (200 μM) alone and in the presence of the complexes, catecholate ligands, and EB (20 μM) in 2% DMSO/Tris buffer (5 mM).

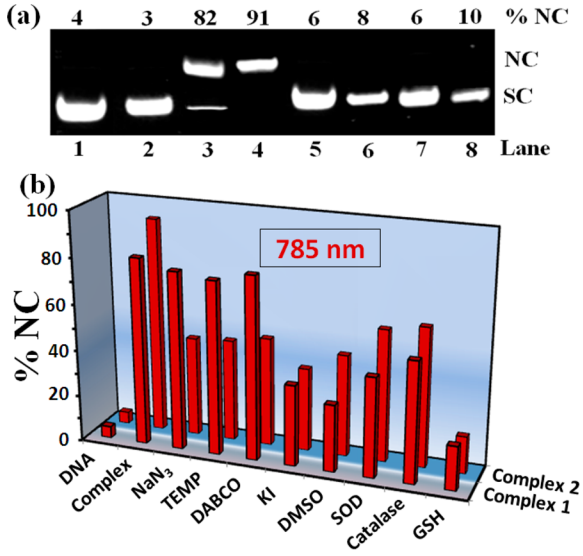

Figure 10. (a) Gel diagram showing pUC19 DNA (0.2 μg, 30 μM base pair) cleavage upon treatment with complexes **1**−**3** (40 μM) in light (785 nm, 1 h exposure) and the dark: lane 1, DNA control (dark); lane 2, DNA control (light); lane 3, DNA + **1** (light); lane 4, DNA + **2** (light); lane 5, DNA + **3** (light); lane 6, DNA + **1** (dark); lane 7, DNA + **2** (dark); lane 8, DNA + **3** (dark). SC is supercoiled DNA, and NC is nicked circular DNA. (b) Bar diagram showing photocleavage of pUC19 DNA (0.2 μg, 30 μM base pair) for complexes **1** and **2** (40 μM) in light of 785 nm (diode laser source with 1 h exposure) in the presence of different additives: NaN_3, 4 mM; TEMP, 4 mM; DABCO, 4 mM; DMSO, 8 μL; KI, 4 mM; SOD, 4 units; catalase, 4 units, GSH, 10 mM. The incubation time was 1 h.

The an-cat and py-cat complexes and corresponding ligands showed partial intercalative modes of binding to ct-DNA, while complex **3** displayed only groove binding propensity. The thermal denaturation experiments were also carried out to find the melting temperatures (T_m) of ct-DNA (200 μM) in the presence and absence of the complexes (20 μM; Figure 9b and Table2). The molecules with the ability to intercalate between the DNA base pairs increase the thermal stability of duplex DNA with an increase of the melting temperature (ΔT_m). EB as a classical DNA intercalator showed a ΔT_m value of 11 °C under similar conditions. The ΔT_m values of 3.3 and 5.3 °C for **1** and **2**, respectively, indicate partial intercalative binding of the complexes to ct-DNA. Complex **3** showed a ΔT_m value of 2 °C, indicating the groove binding nature of the complex. The viscometric experiments further confirmed the partial intercalative properties of complexes **1** and **2** with ct-DNA. The viscosity of the DNA duplex is altered upon interaction with intercalators, the surface, and groove binders. When the viscosity profile of the complexes is compared with those of EB as an intercalator and Hoechst dye as a groove binder, it is observed that complexes **1** and **2** bind to DNA in an intercalative manner, while complex **3** shows a groove binding mode, as seen for the Hoechst dye (Figure S47 in the SI).

DNA Cleavage. The complexes of two catecholate derivatives exhibited significant DNA binding interactions. We thus explored their DNA photocleavage properties using SC pUC19 DNA and red light from a diode laser source of 785 nm (Figure 10a). The choice of the excitation wavelength was based on the presence of a visible band near 770 nm. The gel diagram showed significant photocleavage of DNA in red light by both **1** and **2** (40 μM). Complex **1** showed the formation of ∼82% of nicked circular (NC) DNA, while complex **2** showed ∼93% cleavage of SC DNA. The free ligands H_2an-cat and H_2py-cat failed to show any significant photoinduced DNA cleavage activity in red light in the absence of any intense absorption band around this wavelength (Figure S48 in the SI). The complexes did not show any DNA cleavage activity in the dark.

Mechanistic Aspects. To elucidate the nature of ROS involved, DNA photocleavage experiments were performed in the presence of several quenchers and scavengers like NaN_3, TEMP, and DABCO as singlet oxygen quenchers, KI and DMSO as hydroxyl radical scavengers, catalase as a H_2O_2 scavenger, and superoxide dismutase (SOD) as a superoxide radical scavenger and also in the presence of reducing GSH. From the bar diagram shown in Figure 10b (Figure S48 in the SI), it is apparent that the photoinduced DNA cleavage activity of complex **1** gets reduced from 80% to 20% of NC DNA in the presence of hydroxyl radical scavengers, while for **2**, the NC DNA formation gets significantly suppressed (by almost 35%) in the presence of both singlet oxygen and hydroxyl radical quenchers. The results indicate hydroxyl radical formation for complex **1**, while complex **2** involves both singlet oxygen and hydroxyl radicals as ROS. The addition of excess GSH (10 mM) suppressed the DNA cleavage activity to almost 17%. This indicates that the complexes upon reaction with GSH possibly lead to loss of the intense band in the near-IR region, hence resulting in no cleavage of pUC19 DNA.

4. CONCLUSIONS

In summary, 2-(phenylazo)pyridylplatinum(II) catecholates are shown to act as prodrugs and offer a novel strategy to deliver a {(pap)Pt^{II}} species along with the release of catechol derivatives as photocytotoxic agents within the cells upon reduction by cellular GSH (Scheme S3 in the SI). The PDT effect of complex **1** with a 10-fold enhancement of cytotoxicity in HaCaT and MCF-7 cells in visible light of 400−700 nm is a

dx.doi.org/10.1021/ic502317z | Inorg. Chem. 2015, 54, 253−264

significant result. The IC_{50} value of ~5.2 μM of **1** in light compares well to the IC_{50} value of 3.3 μM of PDT-inactive cisplatin in the dark over a long incubation time. Complex **1** containing an anthracenyl group as the photosensitizer is more active than the pyrenyl analogue **2**, which indicates that the different photophysical properties exhibited by planar aromatic moieties in a biological medium are crucial in governing their photocytotoxic behavior. This study clearly shows how a photoactive catecholate species can be readily delivered in a unique way into the cellular medium triggered by the intracellular GSH having a reducing thiol group. Such a process is clearly facilitated by the platinum(II)-bound 2-phenylazopyridine ligand, which is well-known for its redox properties generating radical species. The delivery of such photoactive catechol species to the cellular target is a challenging task in the presence of various scavengers in the biological system. Another important observation is that the fluorophore-bearing complexes **1** and **2** and the corresponding ligands H_2an-cat and H_2py-cat localize predominantly within the nucleus, and the DNA binding results show the intercalative interactions with the DNA. Besides, they show significant DNA photocleavage activity in red light involving ROS. Complex **1** with its remarkable PDT effect could serve as a potential single prodrug to generate a dual-action platinum-based anticancer agent for combination therapy. This work is likely to presage the design and synthesis of metal-based photochemotherapeutic agents showing the release of constituents for enhanced anticancer activity by chemical and/or photochemical means.

■ ASSOCIATED CONTENT

Supporting Information

CIF file giving crystallographic data for **3**, IC_{50} values in MCF-7 and HaCaT cells (Table S1), initial rates (Table S2), energy-minimized coordinates (Table S3), excited-state transitions (Table S4), synthetic schemes (Schemes S1 and S2), mechanistic aspects (Scheme S3), ligand characterization data (Figures S1−S6 and S16), complex characterization data (Figures S7−S15 and S17), MTT assays (Figures S18−S20), cellular data (Figures S21−S28 and S43−S45), complex stability in the presence of different analytes in the dark and light (Figures S29−S41), optimized structures and molecular orbital pictures (Figure S42), DNA binding and cleavage (Figures S46−S48), and data/experimental details as described in the text. This material is available free of charge via the Internet at http://pubs.acs.org.

■ AUTHOR INFORMATION

Corresponding Authors

*E-mail: paturu@mrdg.iisc.ernet.in. Tel.: +91-80-22933259.
*E-mail: arc@ipc.iisc.ernet.in. Tel.: +91-80-22932533.

Notes

The authors declare no competing financial interest.

■ ACKNOWLEDGMENTS

We thank the Department of Science and Technology (DST), Government of India, and the Council of Scientific and Industrial Research (CSIR), New Delhi, India, for financial support (Grants SR/S5/MBD-02/2007 and CSIR/01(2559)/12/EMR-II/2012). A.R.C. thanks the DST for a J. C. Bose National Fellowship and the Alexander von Humboldt Foundation, Bonn, Germany, for donation of an electrochemical system. We thank Ms. Uttara Basu for her help in ligand synthesis. We are thankful to Drs. O. Joy, P. Pai, and A. Kavya for FACS analysis and Deepti Bapat for the confocal and fluorescence microscopy data. We thank Dr. R. Chakrabarti, Centre for Earth Sciences, of our institute for the ICP-MS facility.

■ REFERENCES

(1) Mjos, K. D.; Orvig, C. *Chem. Rev.* **2014**, *110*, 4540−4563.
(2) Postiglione, I.; Chiaviello, A.; Palumbo, G. *Cancers* **2011**, *3*, 2597−2629.
(3) Hait, W. N. *Nat. Rev. Drug Discovery* **2010**, *9*, 253−254.
(4) Wang, X.; Guo, Z. *Chem. Soc. Rev.* **2013**, *42*, 202−224.
(5) Gabano, E.; Ravera, M.; Osella, D. *Dalton Trans.* **2014**, *43*, 9813−9820.
(6) Wheate, N. J.; Walker, S.; Craig, G. E.; Oun, R. *Dalton Trans.* **2010**, *39*, 8113−8127.
(7) Dhar, S.; Lippard, S. J. *Proc. Natl. Acad. Sci. U. S. A.* **2009**, *52*, 22199−22204.
(8) Johnstone, T. C.; Wilson, J. J.; Lippard, S. J. *Inorg. Chem.* **2013**, *52*, 12234−12249.
(9) Suntharalingam, K.; Song, Y.; Lippard, S. J. *Chem. Commun.* **2014**, *50*, 2465−2468.
(10) Marrache, S.; Pathak, R. K.; Dhar, S. *Proc. Natl. Acad. Sci. U. S. A.* **2014**, *111*, 10444−10449.
(11) Dhar, S.; Kolishetti, N.; Lippard, S. J.; Farokhzad, O. C. *Proc. Natl. Acad. Sci. U. S. A.* **2011**, *5*, 1850−1855.
(12) Zheng, Y.-R.; Suntharalingam, K.; Johnstone, T. C.; Yoo, H.; Lin, W.; Brooks, J. G.; Lippard, S. J. *J. Am. Chem. Soc.* **2014**, *136*, 8790−8798.
(13) Pathak, R. K.; Marrache, S.; Choi, J. H.; Berding, T. B.; Dhar, S. *Angew. Chem., Int. Ed.* **2014**, *53*, 1−6.
(14) Chin, C. F.; Yap, S. Q.; Li, J.; Pastorin, G.; Ang, W. H. *Chem. Sci.* **2014**, *5*, 2265−2270.
(15) Yuan, Y.; Kwok, R. T. K.; Tang, B. Z.; Liu, B. *J. Am. Chem. Soc.* **2014**, *136*, 2546−2554.
(16) Farrer, N. J.; Woods, J. A.; Munk, P. V.; Mackay, F. S.; Sadler, P. J. *Chem. Res. Toxicol.* **2010**, *23*, 413−421.
(17) Zhao, Y.; Woods, J. A.; Farrer, N. J.; Robinson, K. S.; Pracharova, J.; Kasperkova, J.; Novakova, O.; Li, H.; Salassa, L.; Pizarro, A. M.; Clarkson, G. J.; Song, L.; Brabec, V.; Sadler, P. J. *Chem.—Eur. J.* **2013**, *19*, 9578−9591.
(18) Butler, J. S.; Woods, J. A.; Farrer, N. J.; Newton, M. E.; Sadler, P. J. *J. Am. Chem. Soc.* **2012**, *134*, 16508−16511.
(19) Saczko, J.; Mazurkiewicz, M.; Chwilkowska, A.; Kulbacka, J.; Kramer, G.; Ługowski, M.; Śnietura, M.; Banas, T. *Folia Biol. (Praha)* **2007**, *53*, 7−12.
(20) Bonnett, R. *Chemical Aspects of Photodynamic Therapy*; Gordon & Breach: London, U.K., 2000.
(21) Celli, J. P.; Spring, B. Q.; Rizvi, I.; Evans, C. L.; Samkoe, K. S.; Verma, S.; Pogue, B. W.; Hassan, T. *Chem. Rev.* **2010**, *110*, 2795−2838.
(22) Ethirajan, M.; Chen, Y.; Joshi, P.; Pandey, R. K. *Chem. Soc. Rev.* **2011**, *40*, 340−362.
(23) Higgins, S. H. L.; Brewer, K. J. *Angew. Chem., Int. Ed.* **2012**, *51*, 11420−11422.
(24) Maity, B.; Gadadhar, S.; Goswami, T. K.; Karande, A. A.; Chakravrty, A. R. *Eur. J. Med. Chem.* **2012**, *57*, 250−258.
(25) Mitra, K.; Basu, U.; Khan, I.; Maity, B.; Kondaiah, P.; Chakravarty, A. R. *Dalton Trans.* **2014**, *43*, 751−763.
(26) Thiabaud, G.; Arambula, J. F.; Siddik, J. H.; Sessler, J. L. *Chem.—Eur. J.* **2014**, *20*, 8942−8947.
(27) Naik, A.; Rubbiani, R.; Gasser, G.; Spingler, B. *Angew. Chem., Int. Ed.* **2014**, *53*, 6938−6941.
(28) Oretga, A. L.; Mena, S.; Estrela, J. M. *Cancers* **2011**, *3*, 1285−1310.
(29) Wu, X.; Sun, X.; Guo, Z.; Tang, J.; Shen, Y.; James, T. D.; Tian, H.; Zhu, W. *J. Am. Chem. Soc.* **2014**, *136*, 3579−3588.

(30) Doughan, S. J.; Habtemariam, A.; McHale, S. E.; Parsons, S.; Sadler, P. J. *Proc. Natl. Acad. Sci. U. S. A.* **2008**, *105*, 11628−11633.
(31) Dougan, S. J.; Melchart, M.; Habtemariam, A.; Parsons, S.; Sadler, P. J. *Inorg. Chem.* **2006**, *45*, 10882−10894.
(32) Fu, Y.; Habtemariam, A.; Pizarro, A. M.; van Rijt, S. H.; Healey, D. J.; Cooper, P. A.; Shnyder, S. D.; Clarkson, G. J.; Sadler, P. J. *J. Med. Chem.* **2010**, *53*, 8192−8196.
(33) Perrin, D. D.; Armarego, W. L. F.; Perrin, D. R. *Purification of Laboratory Chemicals*; Pergamon Press: Oxford, 1980.
(34) (a) Faessinger, R. W.; Brown, E. V. *J. Am. Chem. Soc.* **1951**, *73*, 4606−4608. (b) Rauth, G. K.; Pal, S.; Das, D.; Sinha, C.; Slawin, A. M. Z.; Woollins, J. D. *Polyhedron* **2001**, *20*, 363−372.
(35) Walker, N.; Stuart, D. *Acta Crystallogr., Sect. A* **1983**, *A39*, 158−166.
(36) Sheldrick, G. M. *Acta Crystallogr., Sect. A* **2008**, *64*, 112−122.
(37) Johnson, C. K. *ORTEP, Report ORNL-5138*; Oak Ridge National Laboratory: Oak Ridge, TN, 1976.
(38) Frisch, M. J. et al. *Gaussian 09*, revision A.1; Gaussian, Inc.: Wallingford, CT, 2009 (see the SI for the full citation).
(39) (a) Becke, A. D. *Phys. Rev. A* **1988**, *38*, 3098−3100. (b) Becke, A. D. *J. Chem. Phys.* **1993**, *98*, 5648−5652. (c) Lee, C.; Yang, W.; Parr, R. G. *Phys. Rev. B: Condens. Matter* **1988**, *37*, 785−789.
(40) Tomasi, J.; Persico, M. *Chem. Rev.* **1994**, *94*, 2027−2094.
(41) McGhee, J. D.; von Hippel, P. H. *J. Mol. Biol.* **1974**, *86*, 469−489.
(42) Carter, M. T.; Rodriguez, M.; Bard, A. J. *J. Am. Chem. Soc.* **1989**, *111*, 8901−8911.
(43) Geary, W. J. *Coord. Chem. Rev.* **1971**, *7*, 81−122.
(44) Panda, M.; Das, S.; Mostafa, G.; Casteneiras, A.; Goswami, S. *Dalton Trans.* **2005**, 1249−1255.
(45) Patai, S, Ed. *The Chemistry of Hydrazo*; Azo and Azoxy Groups, Wiley: Bristol, U.K., 1975.
(46) Shellaiah, M.; Wu, Y.-H.; Singh, A.; Ramakrishnan-Raju, V. M.; Lin, H.-C. *J. Mater. Chem. A* **2013**, *1*, 1310−1318.
(47) Sun, B.; Yang, Z.; Ma, L.; Niu, C.; Wang, F.; Na, N.; Wen, J.; Ouyang, J. *Langmuir* **2013**, *29*, 1952−1962.
(48) Ding, D.; Li, K.; Liu, B.; Tang, B. Z. *Acc. Chem. Res.* **2013**, *46*, 2441−2453.
(49) Roy, S.; Hartenbach, I.; Sarkar, B. *Eur. J. Inorg. Chem.* **2009**, 2553−2558.
(50) Dogan, A.; Sarkar, B.; Klein, A.; Lissner, F.; Schleid, T.; Fiedler, J.; Zalis, S.; Jain, V. K.; Kaim, W. *Inorg. Chem.* **2004**, *43*, 5973−5980.
(51) Zou, Y.; Lok, C.-N.; Fung, Y. M. E.; Che, C.-M. *Chem. Commun.* **2013**, *49*, 5423−5429.
(52) Mackay, F. S.; Woods, A. J.; Heringova, P.; Kasparkova, J.; Pizzaro, A. M.; Moggach, S. A.; Parsons, S.; Brabec, V.; Sadler, P. J. *Proc. Natl. Acad. Sci. U. S. A.* **2007**, *104*, 20743−20748.
(53) Ricchelli, F. *J. Photochem. Photobiol., B* **1995**, *29*, 109−118.
(54) Jones, G.; Vullev, V. I. J. *Phys. Chem. A* **2001**, *105*, 6402−6406.
(55) Vermes, I.; Haanen, C.; Steffens-Nakken, H.; Reutelingsperger, C. *J. Immunol. Methods* **1995**, *184*, 39−51.
(56) (a) Takanashi, T.; Ogura, Y.; Taguchi, H.; Hashizoe, M.; Honda, Y. *Invest. Ophthalmol. Visual Sci.* **1997**, *38*, 2721−2728. (b) Keston, A. S.; Brandt, R. *Anal. Biochem.* **1965**, *11*, 1−5.
(57) Verschoor, L. M.; Singh, G. *Mol. Cancer* **2013**, *12*, 128.
(58) Wang, X.; Guo, Z. *Anti-Cancer Agents Med. Chem.* **2007**, *7*, 19−34.